GNSS-R ground-based and airborne campaigns for ocean, land, ice, and snow techniques: Application to the GOLD-RTR data sets

E. Cardellach,[1] F. Fabra,[1] O. Nogués-Correig,[1] S. Oliveras,[1] S. Ribó,[1] and A. Rius[1]

Received 22 February 2011; revised 19 July 2011; accepted 20 July 2011; published 25 October 2011.

[1] Several ground-based and airborne data sets taken with the Global Navigation Satellite System Reflectometry (GNSS-R) technique are made available to the research community. This paper reviews the potential applications of these bistatic radar observations, including a list of possible approaches and algorithms described in the literature for oceanic measurements (altimetric and scatterometric), soil moisture sensing, and sea ice and snow characterization. A list of applicable models complements the review. The paper continues with descriptions of the campaigns included in the initial data set, together with the basic information required to understand the instrumental issues of the data. Finally, some parameters and observables provided in the data are detailed.

Citation: Cardellach, E., F. Fabra, O. Nogués-Correig, S. Oliveras, S. Ribó, and A. Rius (2011), GNSS-R ground-based and airborne campaigns for ocean, land, ice, and snow techniques: Application to the GOLD-RTR data sets, *Radio Sci.*, *46*, RS0C04, doi:10.1029/2011RS004683.

1. Introduction

[2] The Global Navigation Satellite Systems Reflectometry (GNSS-R) technique, also known as the Passive Reflectometry and Interferometry (PARIS) technique, was suggested by *Martín-Neira* [1993] as source of opportunity for altimetric measurements (Figure 1). As reviewed in section 3, the list of potential applications has increased considerably since then to include the remote sensing of the sea surface roughness and salinity, the soil moisture, sea ice characterization, and snow structures.

[3] Because of the mostly noncoherent nature of the reflected signals, these cannot usually be tracked by the standard navigation GNSS receivers (GPS, GLONASS, future GALILEO, and COMPASS). In order to conduct experimental work, the GPS Open Loop Differential Real-Time Receiver (GOLD-RTR) was designed and manufactured at the Institut de Ciències de l'Espai [*Nogués-Correig et al.*, 2007]. Since 2005, this GNSS-R hardware receiver has been used in more than 42 campaign flights and for more than 250 days of continuous ground-based observations. A general sketch of its functionality is given in Figure 2. Data have been taken over oceans, land, sea ice, and dry snow. Besides being one of the few dedicated GNSS-R observation set, the data are also quite unique because of the multiple antenna measurements. As detailed in section 5, some of the campaigns were equipped with both copolar and cross-polar antennas, and some others used two cross-polar antennas that might allow advanced interferometric techniques.

[4] Although extensive results have been already obtained with these sets [*Nogués-Correig et al.*, 2007; *Cardellach and Rius*, 2008; *Rius et al.*, 2010; *Cardellach et al.*, 2009; F. Fabra et al., Phase altimetry with dual polarization GNSS-R over sea ice, submitted to *IEEE Transactions on Geoscience and Remote Sensing*, 2011], they still offer many opportunities for research. For instance, to help establishing the error budget of a wide range of GNSS-R techniques.

[5] In particular, the recently launched SMOS [*McMullan et al.*, 2008] and the soon to be launched Aquarius [*Lagerloef et al.*, 2008] L band radiometric space-based missions for ocean salinity monitoring require better understanding of sea surface roughness as bistatically sensed at L band [e.g., *Miranda et al.*, 2003; *Delwart et al.*, 2008]. The L band is sensitive to intermediate scales of the sea wave spectrum. They do not relate directly to the instantaneous wind, but a combination of wind, swell and waves age. It is needed to properly discern between those contributions, as well as to find potential new applications of these intermediate wave scales. This data set provides L band bistatic observations of the sea surface under different sea surface conditions, thus suitable to tackle these topics.

[6] Another important open question is the modeling of the copolar scattering component: the received scattered copolar component (right-hand circular polarization, RHCP) weakly matches the modeled waveforms. Proper models for the copolar component of the scattering must be investigated. This data set provides scattering events at both polarizations, the only set the authors are aware of that include polarimetric reflections, except for the data of *Elfouhaily et al.* [2002].

[7] It has been proved that some GPS transmitters are affected by significant multipath (up to 2 m transmitted multipath delay in SV 49 [*Esterhuizen*, 2010]). Therefore,

[1]Institut de Ciències de l'Espai, CSIC/IEEC, Barcelona, Spain.

0048-6604/11/2011RS004683

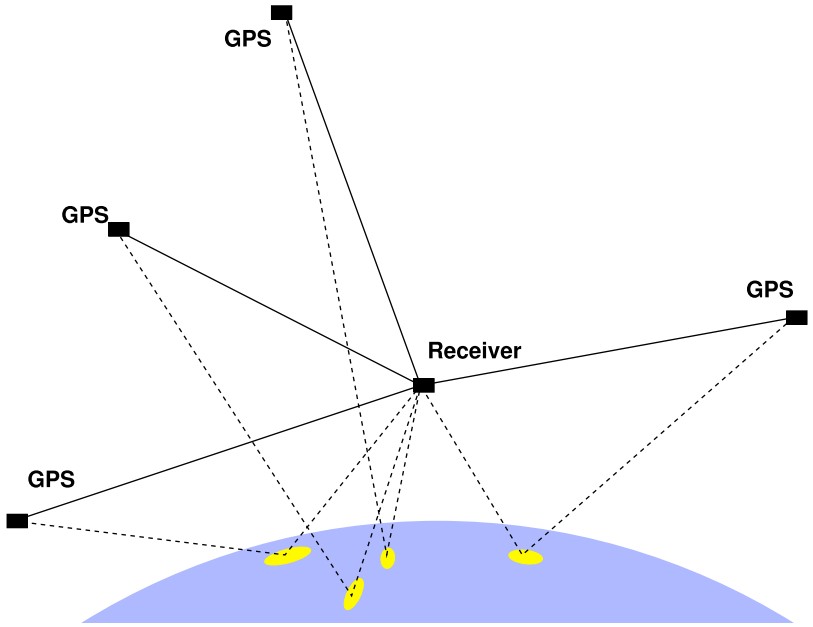

Figure 1. Nonscaled sketch of the Global Navigation Satellite System Reflectometry (GNSS-R) approach. A receiver above the Earth's surface collects the direct signals as well as those reflected off of the surface. They come from areas around the specular points, the glistening zones.

these data sets could also be suitable for studying the impact of the multipath generated at the GPS transmitters onto GNSS-R altimetry and scatterometry.

[8] The data sets are now available to the community, through the Web server http://www.ice.csic.es/research/gold_rtr_mining/. It must be noted that the content of the data includes GNSS-R observables, both raw and up to a certain preprocessing level, but they do not provide the final geophysical products.

[9] This paper compiles a review of their potential applications, lists the algorithms and methods suggested and/or validated in the literature, and gives some details to properly obtain and use the data.

2. Basic GNSS and GNSS-R Concepts

[10] A detailed description of the Global Positioning System is given by *Spilker et al.* [1996] and *Misra and Enge* [2006]. For geoscientists unfamiliar with these navigation systems but who wish to use these data sets for research, the relevant information can be summarized as follows: a low signal-to-noise (SNR) L band (we use one of the two available frequencies, L1 = 1575.42 MHz, λ = 0.1905 m wavelength) electromagnetic field is transmitted by satellites orbiting at ~20,000 km altitude. The signals are transmitted at RHCP, continuously. Several codes modulate the signal by introducing 180° phase shifts. One of the codes is the navigation code, used to help real-time positioning. This is not going to be relevant for the user of this data set because the postprocessed transmitter and receiver positions are provided, and the milliseconds of data with a potential navigation bit transition (with thus potential degraded performance) have been removed from the data set. The other codes are designed to isolate the signal transmitted by one particular GPS space vehicle from the others received simultaneously (Code Division Multiple Access, CDMA). To achieve it, the codes take the shape of pseudorandom noise (PRN), sequences of arbitrary phase jumps that when correlated by any other transmitter PRN result in a quasi-null cross-correlation function (orthogonal-like behavior). Therefore, the GPS receiver needs to cross correlate the signal captured by the antenna with replicas of the PRN codes, to discern, identify and separate them. These cross-correlation functions are also called waveforms, or delay maps (DM). The correlation function in direct propagation conditions (no reflection) is ideally a triangle (in amplitude units). The half width of the triangle is the chip length (time interval for potential phase shifts to occur). For the Coarse/Acquisition (C/A) code, used in our data, this is ~300 m. The delay of the signal is measured by either displacements of the peak of this triangle function (group delay), or more precisely by tracking the changes in the phase of the carrier (2π radiant corresponding to 1λ change in the transmitter-receiver distance). The ionospheric and lower atmospheric conditions, together with multipath environment (reflections in objects near the receiving antenna) introduce some additional delays.

[11] When the signal reflected off of the Earth surface is collected, the following occur: (1) The polarization is mostly swapped, from RHCP to left-hand circular polarization (LHCP); this effect depends on the dielectric properties of the surface and the geometry of the reflection. (2) The correlation function is distorted; because of the diffuse scattering, the antenna collects signals reflected at the specular point as well as at other points within the surface (the glistening zone), which add contributions to the cross-correlation function at longer delays than the specular one. The waveform is no longer a triangle function, but the trailing edge decays at lower slope than the leading edge. Moreover, in certain dynamic conditions, the Doppler

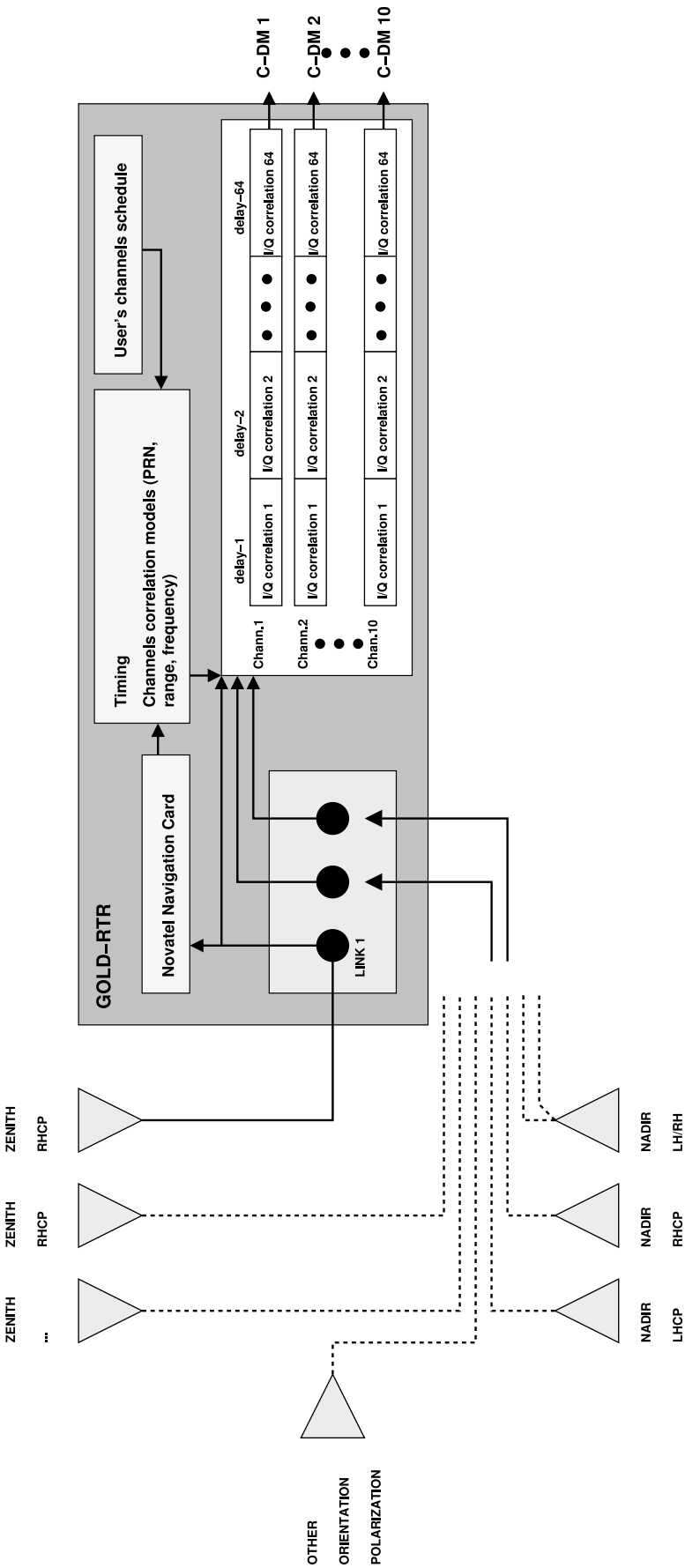

Figure 2. Block diagram of the GPS Open Loop Differential Real-Time Receiver (GOLD-RTR) receiving system. An up-looking right-hand circular polarization (RHCP) antenna must be connected to link 1 to provide navigation and timing. Any other antenna in any polarization can be connected to the rest of the links. The user programs the correlation channels scheduler, deciding which satellites correlate in each correlation channel and under which correlation optional parameters (frequency and/or delay offsets to combine different channels in a single DDM). On the basis of this requirement and the range and frequency information derived from the navigation card, the signal processor performs ten 64-lag complex correlations (C-DM) every millisecond.

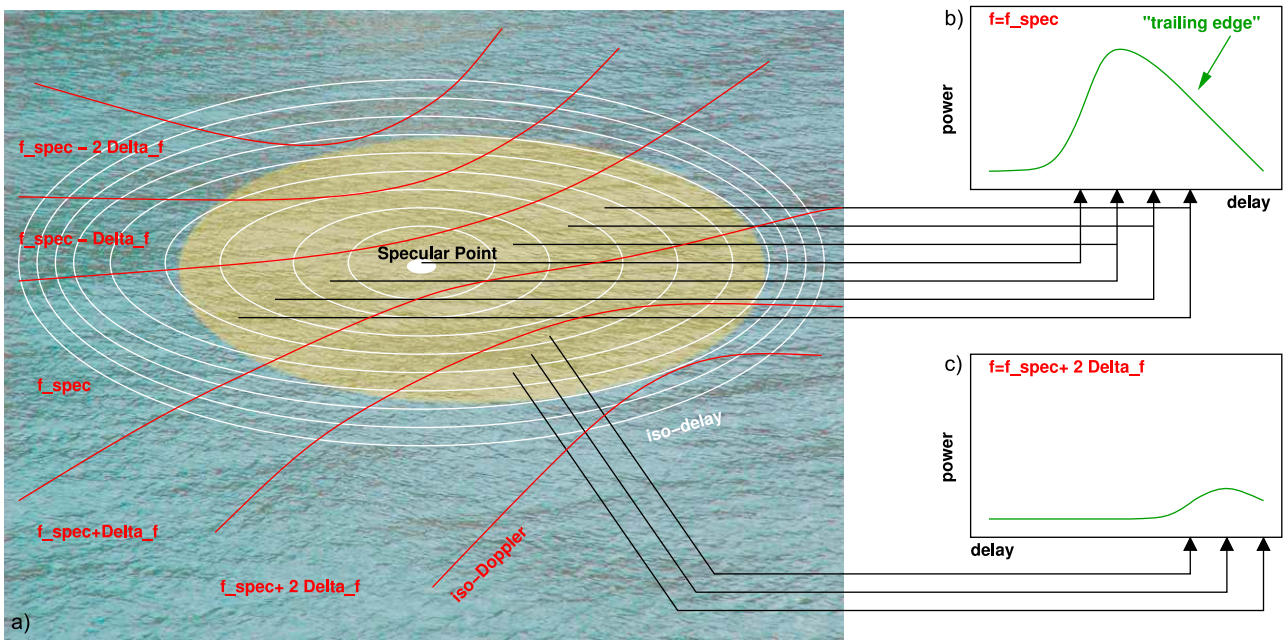

Figure 3. (a) When the glistening zone (area over which the signal is reflected toward the receiver, in green) is wide, the cross-correlation process filters out the contributions reflected with geometric Doppler, significantly different than the specular one (marked in red). Then, the cross correlation can be performed with different frequency corrections to capture the other Doppler belts. Each DM correlation corresponds to a Doppler belt: for example, (b) central DM and (c) $+2\Delta f$. The composition of all the DM slices generates the delay-Doppler map (DDM), as shown in Figure 4.

frequency suffered by the off-specular reflections differs significantly from the Doppler frequency at the specular point. These signals are then filtered out by the cross-correlation and coherent integration process (it depends on the coherent integration time, T_i as $1/T_i$). In those cases to retrieve the complete glistening zone, a set of cross correlations must be performed at slightly different frequencies around the specular one, generating a delay Doppler map (DDM; Figures 3 and 4). All these waveforms can be provided as a set of complex numbers (C-DM, C-DDM), given in amplitude units, or noncoherently integrated in time to reduce the noise, given in power units (P-DM, P-DDM).

3. Review on GNSS-R Applications

[12] The GNSS-R applications tend to be classified according to the observed surface: (1) ocean, (2) land, and (3) ice and snow. Another classification regards the final product: (1) altimetry, (2) roughness, and (3) permittivity parameters (such as temperature, salinity, or humidity, which determine the reflectivity level of the surface materials). Still, the observables used in the technique might also characterize the classification: (1) integrated power observables solely or (2) high sampling complex correlation functions (amplitude and phase). Finally, we might need to distinguish between applications that require polarimetric or nonpolarimetric observables. The data obtained in the experimental campaigns cover all the cases. Therefore, from here on this section focuses on the applications that can be tested with the released data set, that is, applications of both integrated and complex field observables, under the surface and final product categories above, either polarimetric or not. Table 1 codifies and summarize the techniques, it also provides the reference literature for each method as well as the required type of data.

3.1. Altimetry

[13] The altimetric techniques can in principle be applied to reflections off any surface, but their performance will depend on the signal-to-noise ratio of the scattering. Therefore, GNSS-R altimetry has only been conducted on strongly reflecting surfaces and geometries, such as waters and smooth ice, or land at near-surface receiver altitudes [*Rodriguez-Alvarez et al.*, 2011].

[14] The altimetry aims to resolve the vertical distance between the receiver and the surface and/or the vertical location of the specular point (with respect to a reference ellipsoid or geoid). Both quantities are related as pictured in Figure 5. The observables to deal with are the distances between transmitter, receiver, and/or surface. They can be given in the space domain (called ranges) or in the time domain (called delays). They are related to each other by the speed of light, and from here on we will call them range or delays indistinctly. Because the GNSS-R observations are bistatic, the way to relate the ranges with the surface level will depend on the geometry (incidence angle), as well as other systematic effects (atmospheric, instrumental, antennas set up, etc.). All these questions are tackled in section 4, which is devoted to models. Here we focus on the observable, that is, the altimetric range. The altimetric range is the distance traveled by the reflected signal with respect to the one traveled by the direct radio link. When the range is measured through the delay of the code (delay of the correlation function), it tends to be called group delay or

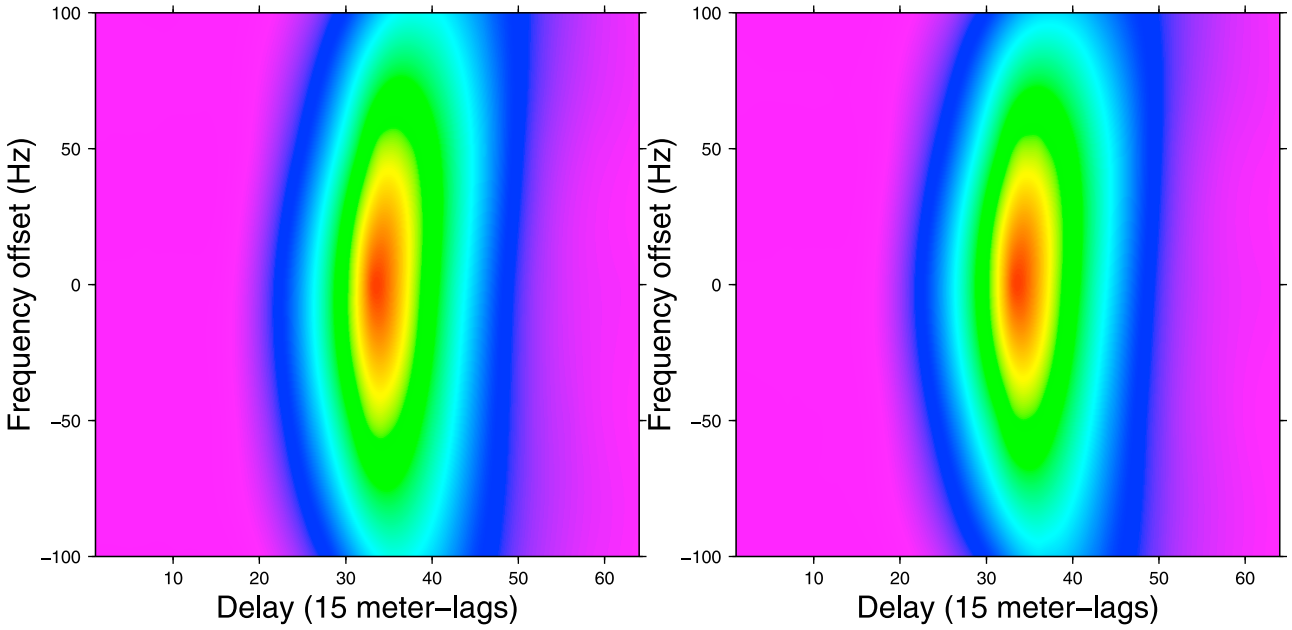

Figure 4. (left) An example of 10 ms coherently and up to 1 s noncoherently averaged DDM as received through the combination of five channels of correlation. (right) DDM synthesised using the 1 KHz time series of raw data corresponding to the central frequency slice in Figure 4 (left). The procedure is explained in Table 2, here using 10 ms coherent integration and up to 1 s noncoherent integration. A linear color scale is used for power (the same for both plots, in arbitrary units). These DDMs are not fully equivalent because of the frequency filtering suffered by the raw data used to synthesize the DDM in Figure 4 (right) (filtering in *sinc* shape during their 1 ms integration process).

pseudorange. When the carrier phase can be tracked, variations in the range can be monitored with much better precision, since an entire cycle corresponds to $\lambda \sim 20$ cm change (~0.5 mm/carrier phase degree). This latter approach is called carrier phase altimetry.

3.1.1. Group Delay Altimetry Observables

[15] In a smooth-surface reflection event, the distance between the path traveled by the reflected signal and the path traveled by the direct link would simply correspond to the range between the peaks of the two correlation functions. Nevertheless, and since most reflections occur off rough surfaces, this approach cannot generally be used (*Rius et al.* [2002] show that variations in the delay of the reflected peak mostly account for changes in the surface roughness). Figure 6 shows the ranges involved in altimetry, as given in this data set.

[16] A few techniques have been used to identify the specular point delay in the waveform.

[17] 1. For Peak-Delay (AG.P) the altimetric range is taken as the peak-to-peak delay. This peak delay can be directly extracted by combining some fields provided in the data (see Table 2).

[18] 2. Retracking (AG.R) consists of fitting a theoretical model to the data. The best fit model indicates the delay where the specular point lies.

[19] 3. Peak-Derivative (AG.D) identifies the maximum of the derivative of the leading edge as the specular point delay. The peak derivative delay can be directly extracted by combining some fields provided in the data (see Table 2).

[20] See Tables 1 and 2 for completeness.

3.1.2. Phase Delay Altimetry Observables

[21] The phase at which the direct and reflected signals (ϕ_d and ϕ_r, respectively) reach the receiver depends on the range between the transmitter and the direct and reflected antenna phase centers (r_d and r_r), respectively, through the terms $\phi_d \propto k \cdot r_d$ and $\phi_r \propto k \cdot r_r$, where k states for the carrier's wave number. The reflected phase, given with respect to the direct one, thus becomes $\phi_{r-d} \propto k \cdot (r_r - r_d)$, where $(r_r - r_d)$ is the altimetric range, r_{r-d}. The phase delay altimetry approach aims to measure the altimetric range by means of carrier phase observations ϕ_{r-d}. When the signals reflect off rough surfaces, the received phase ϕ_r becomes too noisy (noncoherent) and the technique cannot be applied.

[22] In general, it can be used in very smooth surfaces (some ice surfaces [*Gleason*, 2006]), from very low altitudes (a few meters), and over very slant geometries (a few degrees in elevation). Some of the released data sets are suitable for phase altimetry (see Table 3), using the following techniques below (also summarized in Table 1).

[23] 1. For Interferometric beats (AP.I), when the altitude is low enough or the observation at grazing angles, the delay between the reflected and direct signals is short and their correlation functions overlap, producing interference beats. These beats are oscillations of the amplitude and phase of the total field (sum of the two signals), and they occur at the frequency $(1/\lambda)d(r_r - r_d)/dt$. *Cardellach et al.* [2004] obtained phase delay altimetry by analyzing the interferences found in radio-occultation data from the CHAMP low Earth orbiter. Similarly, A. Helm et al. (Detection of coherent reflections with GPS bipath interferometry,

Table 1. List of the Global Navigation Satellite System Reflectometry (GNSS-R) Techniques Identified in the Literature as Suitable to Apply in the Released Data Set

Code	Technique	Sources	Data[a]
		Group Altimetry	
AG.P	Peak-Delay	*Martín-Neira et al.* [2001]	P-DM
AG.R	Retracking	*Lowe et al.* [2002], *Ruffini et al.* [2004]	P-DM
AG.D	Peak-Derivative	*Hajj and Zuffada* [2003], *Rius et al.* [2010]	P-DM
		Phase Altimetry	
AP.I	Interferometric-beats	*Cardellach et al.* [2004], Helm et al. (unpublished manuscript, 2004)	RHCP (low altitude or elevation) C-DM
AP.5P	5-Parameter DM Fit	*Treuhaft et al.* [2001]	RHCP (low altitude or elevation angle) C-DM
AP.SC	Separate Up/Down Channels	Fabra et al. (submitted manuscript, 2011), *Semmling et al.* [2011]	coherent reflected C-DM and direct C-DM
		Ocean Roughness	
OR.DM	DM-fit	*Garrison et al.* [2002], *Cardellach et al.* [2003], *Komjathy et al.* [2004]	P-DM
OR.MDM	Multiple-satellite DM-fit	*Komjathy et al.* [2004]	P-DM simultaneous PRNs
OR.DDM	DDM-fit	*Germain et al.* [2004]	P-DDM
OR.TE	Trailing-edge	*Zavorotny and Voronovich* [2000a], *Garrison et al.* [2002]	P-DM
OR.DDS	Delay and Doppler spread	*Elfouhaily et al.* [2002]	P-DM, P-DDM
OR.SD	Scatterometric-delay	*Nogués-Correig et al.* [2007], *Rius et al.* [2010]	P-DM
OR.AV	DDM Area/Volume	*Marchan-Hernandez et al.* [2008], *Valencia et al.* [2009]	P-DDM
OR.PDF	Discrete-PDF	*Cardellach and Rius* [2008]	P-DM (isotropic) P-DDM (anisotropic and assymetric)
OR.CT	Coherence-time	*Soulat et al.* [2004], *Valencia et al.* [2010]	Direct and Reflected C-DM low altitude and/or calm waters
		Ocean Permittivity	
OP.PR	Polarimetric-ratio	see Figure 7	Reflected RHCP and LHCP P-DM
OP.POPI	POPI	Cardellach et al. (unpublished manuscript, 2006)	Reflected RHCP and LHCP C-DM
		Land	
L.SMC	Soil-moisture cross-polar	*Masters et al.* [2004], *Manandhar et al.* [2006], *Katzberg et al.* [2005], *Cardellach et al.* [2009]	P-DM and direct P-DM if calibration wanted
L.SMP	Soil-moisture polarimetric-ratio	*Zavorotny and Voronovich* [2000b], *Zavorotny et al.* [2003]	reflected RHCP and LHCP P-DM
L.OI	Object-identification	*Lie-Chung et al.* [2009]	RHCP and LHCP C-DM
		Sea Ice	
I.PP	Permittivity by peak-power	*Komjathy et al.* [2000], *Belmonte* [2007]	P-DM
I.VHP	1st-year thickness VH-phase	*Zavorotny and Zuffada* [2002]	reflected RHCP and LHCP C-DM
I.PR	Permittivity polarimetric ratio	see Figure 8	reflected RHCP and LHCP C-DM
I.POPI	Permittivity POPI	*Cardellach et al.* [2009; unpublished manuscript, 2006]	reflected RHCP and LHCP C-DM
I.R	Sea-Ice roughness	*Belmonte* [2007]	reflected P-DM
		Snow	
S.V	Volumetric-scattering	*Wiehl et al.* [2003]	P-DM or P-DDM

[a]Type of data required to perform the technique. RHCP, right-hand circular polarization; LHCP, left-hand circular polarization; PRN, pseudorandom noise.

unpublished manuscript, 2004) used an equivalent approach to perform phase delay altimetry off of an Alpine lake.

[24] 2. For 5-Parameter DM Fit (AP.5P), a more robust fit is performed by *Treuhaft et al.* [2001], who use the whole complex RHCP (direct + reflected) waveform to extract five parameters, among them the altimetric range.

[25] 3. For Separate Up/Down Channels (AP.SC), when the delay between the two radio links is longer and their correlation functions do not or just weakly overlap, Fabra et al. (submitted manuscript, 2011) and *Semmling et al.* [2011] used separate up and down channels to measure the relative phase ϕ_{r-d}, obtaining sea ice phase altimetry which clearly reproduced the tidal signatures.

3.2. Ocean Surface

3.2.1. Ocean Wind and Roughness

[26] As the GNSS link reflects off the sea surface, its roughness might scatter the signal in a wide range of output directions. As a result, the reflection is not specular (mirror-like), but it spreads in a scattering pattern: contribution from sea surface patches (facets) that have different orientation deviate the signals, and introduce further delays (longer raypath distances than the nominal transmitter-specular-receiver radio link). This changes the properties of the received signal and thus those of its correlation function. In general, the reflected waveforms present lower amplitudes when roughness increases, and the shape is also distorted:

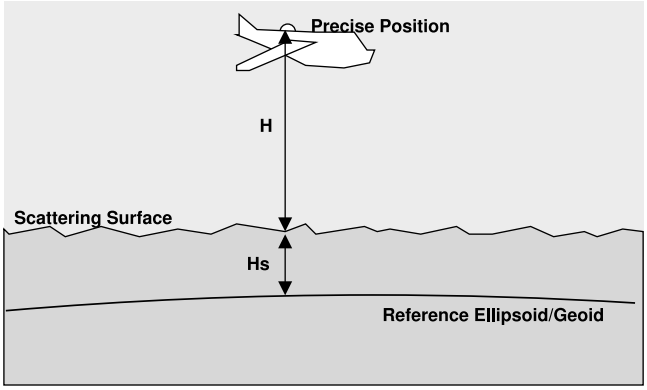

Figure 5. The altimetry resolves the altitude of the receiver above the surface H, from which the surface level H_s can be obtained once the receiver has been precisely positioned by using standard GNSS techniques.

the leading edge (before peak) elongates, the peak gets further delayed, and the trailing edge (after peak) persists longer, with slower decay rate. Information about the surface roughness can be obtained from the analysis of these distortions.

[27] The L band navigation signals, of ~0.2 m electromagnetic carrier wavelength are not sensitive to sea surface roughness of spatial scales much smaller than the electromagnetic wavelength (such as wind instantaneously induced ripple). As a consequence, the GNSS-R ocean scattering observations can inform about intermediate roughness scales, which do not necessarily relate to the wind conditions. One of the open questions is a better understanding and modeling of this roughness term [e.g., *Delwart et al.*, 2008], and researchers are encouraged to use this data set for these investigations. Two L band radiometers have recently been or will soon be launched, SMOS and Aquarius, respectively, which will provide sea surface salinity and soil moisture measurements. Because of them, it is nowadays essential to understand and properly model the L band roughness, and the bistatic scattering of L band signals off the Ocean. The reason is that these issues are required for the proper modeling of the L band emissivity, and the separation between the effects of the permittivity of the surface (salinity and temperature) and the roughness corrections.

[28] The approaches to untangle roughness information that have been identified in the literature as suitable for being applied to this data set are codified and summarized in Table 1. Brief explanations are as follows.

[29] 1. For DM-fit (OR.M), after renormalizing and realigning the delay waveform, the best fit against a theoretical model gives the best estimate for the geophysical and instrumental correction parameters [e.g., *Garrison et al.*, 2002]. Depending on the model used for the fit, the geophysical parameters can be 10 m altitude wind speed, or sea surface slopes' variance (mean square slopes, MSS). Note that the provided data sets, the time delay alignment

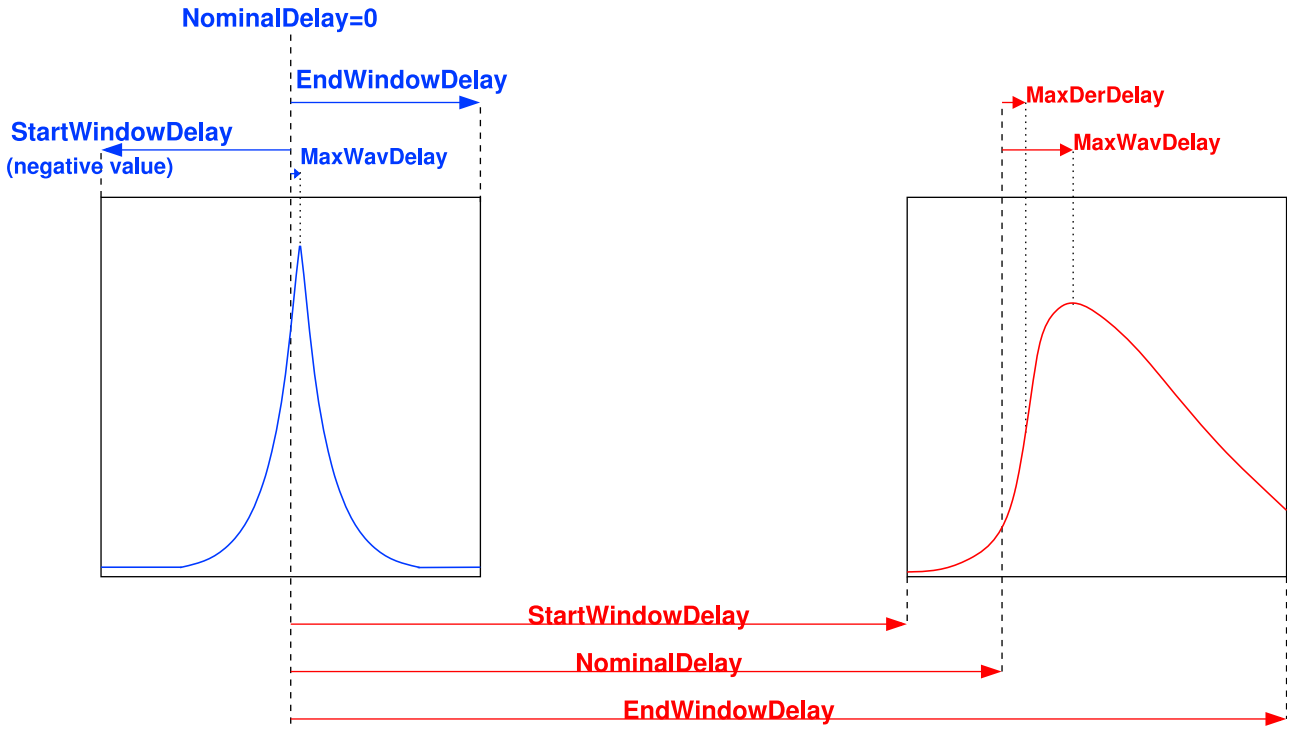

Figure 6. Ranges involved in this GNSS-R data set. The reference range is the NominalDelay of the direct signal (set to zero). MaxWavDelay and MaxDerDelay are always referred to their respective NominalDelay (direct and reflected). The delay of the reflection specular point with respect to the direct reception is given by NominalDelay (reflected) + MaxDerDelay (reflected) − MaxWavDelay (direct). See Tables 2 and 4 for completeness.

Table 2. Construction of Some Basic Observables From netCDF Data Variables

Observables	Construction
DM	Data in the variable array Waveform, the interlag (sampling) distance in (EndWindowDelay − StartWindowDelay)/(N − 1), where N is the number of lags (current instrumental settings are N = 64, 15 m interlag delay). It can be referred to the specular point delay, with its delay given by MaxDerDelay.
DDM	Measured: It is necessary to identify several Channel with the same PRN, Link, and Polarization and different DeltaFreq values within the same SecondOfWeek (in integrated data) or within the same Millisecond (in raw data). Then, the contents of the Waveform from each DeltaFreq corresponds to each frequency slice of the DDM (see Figure 4, left). Synthetic: When the Doppler spread across the glistening area is within 1 kHz, the DDMs can be obtained from raw DM (at central frequency). This applies in most of the released data, and therefore, it also extends the DDM monitoring to those moments in which only DMs were captured. The DDMs can be synthesized by coherently integrating the raw DM while counterrotating the phase by the desired Δf. An example is given in Figure 4 (right).
Peak delay	The delay of the peak with respect to the direct signal is given by NominalDelay (reflected) + MaxWavDelay (reflected) − MaxWavDelay (direct) (in m).[a,b]
Specular delay or altimetric range	The delay of the specular point with respect to the direct signal is given by NominalDelay (reflected) + MaxDerDelay (reflected) − MaxWavDelay (direct) (in m).[a,b]
Scatterometric delay	The delay of the peak with respect to the specular point delay is given by MaxWavDelay (reflected) − MaxDerDelay (reflected) (in m).[b]
Interlag distance	The distance between two subsequent samples is given by (EndWindowDelay − StartWindowDelay)/(N − 1), where N is the total number of lags.

[a]The term WavMaxDelay (direct) can be neglected.
[b]It might fail at low altitudes and/or when reflected and direct signals overlap (CoSMOS 2007, GPS-SI, GPS-DS).

between the data and the model, realignment, is given by the variable MaxDerDelay (see Table 4 and Figure 6), which identifies the specular point.

[30] 2. Multiple-satellite DM-fit (OR.MDM) extends the DM-fit inversion to several simultaneous satellite reflection observations, which resolves the anisotropy (wind direction or directional roughness [*Komjathy et al.*, 2004]).

[31] 3. For DDM-fit (OR.DDM) the fit is performed on a delay Doppler waveform [*Germain et al.*, 2004]. In this way, anisotropic information can be obtained from a single satellite observation.

[32] 4. For Trailing-edge (OR.TE), as suggested from theoretical models of *Zavorotny and Voronovich* [2000a], *Garrison et al.* [2002] implement in real data a technique in which the fit is performed on the slope of the trailing edge, given in dB.

[33] For Delay and Doppler spread (OR.DDS), *Elfouhaily et al.* [2002] developed a stochastic theory that results in two algorithms to relate the sea roughness conditions with the Doppler spread and the delay spread of the reflected signals.

[34] 5. For Scatterometric-delay (OR.SD), for a given geometry, the delay between the range of the specular point and the range of the peak of the reflected delay waveform is nearly linear with MSS. This fact is used to retrieve MSS [*Nogués-Correig et al.*, 2007]. The scatterometric delay can be directly obtained in our data set by combining some of the provided fields (see Table 2 and Figure 6).

[35] 6. For DDM Area/Volume (OR.AV), simulation work by *Marchan-Hernandez et al.* [2008] indicates that the volume and the area of the delay Doppler maps are related to the changes in the brightness temperature of the ocean induced by the roughness. The hypothesis has been experimentally confirmed by *Valencia et al.* [2009].

[36] 7. For Discrete-PDF (OR.PDF), when the bistatic radar equation for GNSS signals is reorganized in a series of terms, each depending on the surface's slope s, the system is linear with respect to the probability density function (PDF) of the slopes. Discrete values of the PDF(s) are therefore obtained. This retrieval does not require an analytical model for the PDF (no particular statistics assumed). In particular,

Table 3. Current Available Campaigns[a]

Name	Funding Agency	Geographical Area	Flights	Ground	H	State	Reflection Polarization	Application
GOLD-TEST	IEEC	Mediterranean Sea	3	–	10	O/L	LH + LH	AG, OR
		Ebre River Delta (Spain)					LH + RH	AG, OR, OP, L.SMC
CoSMOS06	ESA	North Sea (Norway)	12	–	3	O	LH + RH	AG, OR, OP
CoSMOS07	ESA	Baltic Sea (Finland)	2	–	0.3	O	LH + LH	AG, AP.SC, OR, L.SMC
SMOS-RC08	ESA	Baltic Sea	12	–	2–3	O/L	LH + RH	AG, OR, OP
		Germany, France					LH + RH, LH	L.SMC, L.SMP, AP.SC
		Mediterranean Sea, Spain					LH	AG, OR, L.SMC
CAROLS07	CNES	Atlantic, France	3	–	3	O/L	LH + RH	AG, OR, OP, L.SMC, L.SMP
CAROLS09	CNES	Atlantic, Mediterranean, France, Spain	11	–	3–5	O/L	LH + RH	AG, OR, OP, L.SMC, L.SMP
GPS-SIDS-SI	ESA	Disko Bay (Greenland)	–	8 months	0.7	L/I/S	LH + RH	I, AG, AP, OR.DM, OR.MDM, OR.TE, OR.SD, OR.CT, OP L
GPS-SIDS-DS	ESA	Dome C (Antarctica)	–	10 days	0.045	S	LH + RH	S

[a]H is the nominal altitude of the receiver (in km). State indicates states for the reflecting surfaces (ocean (O), land (L), ice (I), and snow(S)). Reflection polarization indicates the polarization of the surface-looking antenna (zenith-looking RHCP is always present). Applicaiton lists the techniques that might potentially be used with each data set (codes are as in Table 1).

Table 4. Some of the netCDF Variables in Integrated Georeferenced Data, Including the Waveform Data, Instrumental Issues, and Models

Name	Units	Level	Description
Record	number	1a	Index that identifies each observation, being an observation the 64-lag output produced every Coherent_int × Uncoherent_int interval by each active correlation channel.
Lags	number	1a	Number that identifies which of the 64 correlators in a correlation channel is giving the corresponding waveform power lag.
Waveform	power units	1a	Power of the waveform, given for each correlation lag.
PRN	number	1a	Number that identifies each one of the orthogonal codes used to modulate the transmitted GPS signals. Each code number corresponds to a particular satellite.
DeltaFreq	Hertz	1a	Offset frequency applied in the correlation, with respect to the specular Doppler frequency. A DDM is produced by the concatenation of several waveforms of the same PRN, at different DeltaFreq.
Polarization	character	1a	Polarization of the receiving antenna being used in this waveform.
Link	number	1a	Number that identifies the radio frequency front-end feeding the correlation channel which is generating the waveform. This identifies the antenna/polarization.
Channel	number	1a	Number that identifies which of the 10 correlation channels in the GOLD-RTR is used to produce the waveform of this Record.
StartWindowDelay	m	1a	Delay of the first lag in the correlation window, with respect to NominalDelay of the direct signal.
EndWindowDelay	m	1a	Delay of the last lag in the correlation window, with respect to NominalDelay of the direct signal.
NominalDelay	m	1a	GOLD-RTR expected delay of the waveform peak (direct) or specular point (reflected). The direct one is given by the internal Novatel receiver card locked at the direct signal, whereas the reflected one is computed by the GOLD-RTR in real-time based on its positioning knowledge and the reference geoid.
MaxWav	power	1b	Maximum of the power waveform of this Record.
MaxWavDelay	m	1b	Delay of the peak of the waveform with respect to the NominalDelay of this same waveform.
MaxDerDelay	m	1b	Delay of the peak of the derivative of the waveform, with respect to the NominalDelay of this same waveform.
EccentricityDelay	m	1b	Eccentricity delay model for this Record.
AtmosphericDelay	m	1b	Atmospheric delay model affecting the reflected-direct signals, as given in equation (3) and Figure 10 (left).
GeometryDelay	m	1b	Geometric delay model, as given in equation (5) and Figure 10 (right).
SigMaxWavDelay	m	1b	Formal uncertainty of MaxWavDelay, negative values for outliers.
SigMaxDerDelay	m	1b	Formal uncertainty of MaxDerDelay, negative values for outliers.

when the technique is applied on delay Doppler maps, is it possible to obtain the directional roughness, together with other non-Gaussian features of the PDF (such as upwind-downwind separation [*Cardellach and Rius*, 2008]).

[37] 8. Finally, for Coherence-time (OR.CT), when the specular component of the scattering is significant (very low altitude observations, very slant geometries, or relatively calm waters), the coherence time of the interferometric complex field depends on the sea state. It is then possible to develop the algorithms to retrieve significant wave height [*Soulat et al.*, 2004; *Valencia et al.*, 2010].

3.2.2. Ocean Permittivity

[38] Polarimetric measurements are sensitive to the permittivity of the reflecting surface. For the Ocean surface, the permittivity at the L band of the electromagnetic spectrum is essentially given by the salinity and the temperature [*Blanch and Aguasca*, 2004].

[39] For Polarimetric ratio (OP.PR) the ratio between the copolar (RHCP) and the cross-polar (LHCP) Fresnel reflection coefficients differs up to 10% between different salinity conditions (Figure 7, top). The direct inversion of the polarimetric ratio is nevertheless an open question, since it will not only depend on the Fresnel coefficients, but on a more complex scattering process, for which the copolar term is not properly modeled yet.

[40] Similarly, for Polarimetric Phase Interferometry (OP.POPI) the difference between the phase of the complex copolarized and cross-polarized components of the reflected fields (RHCP and LHCP, respectively) depends on the permittivity of the surface (E. Cardellach et al., Technical note on polarimetric phase interferometry (POPI), unpublished manuscript, 2006, Figure 7, bottom). This is simply the phase of the polarimetric interferometric field, complex-conjugate multiplication between the copolar and the cross-polar complex components. The long coherence time, of the order of minutes, of the polarimetric interferometric field, increases significantly the precision of the POPI measurement, which requires a theoretical sensitivity of a few degrees phase. Phase wind-up [*Wu et al.*, 1993] affects twice the POPI phase, and it must be corrected.

[41] The data taken up today with the GOLD-RTR cannot provide absolute POPI values, because of instrumental issues, but they can provide POPI variations. The GOLD-RTR has recently been modified to allow absolute POPI measurements, and the data taken during 2010 (27 flights) and later campaigns, to be posted in the server, will be ready for absolute POPI.

3.3. Land and Hydrological Applications

[42] Several techniques to extract soil moisture information contents can be found in the literature. They are mostly sensitive to the 1–2 cm upper layer [*Katzberg et al.*, 2005].

[43] 1. Soil-moisture cross-polar (L.SMC) uses the LHCP SNR as the observable, from which the surface reflectivity is extracted. It can be normalized by the direct power level or even calibrated with observations over smooth water bodies [e.g., *Masters et al.* 2004].

[44] 2. Soil-moisture polarimetric-ratio (L.SMP) is a method that assumes that the received signal power is proportional to the product of two factors: a polarization sensitive factor dependent on the soil dielectric properties and a polarization insensitive factor that depends on the surface

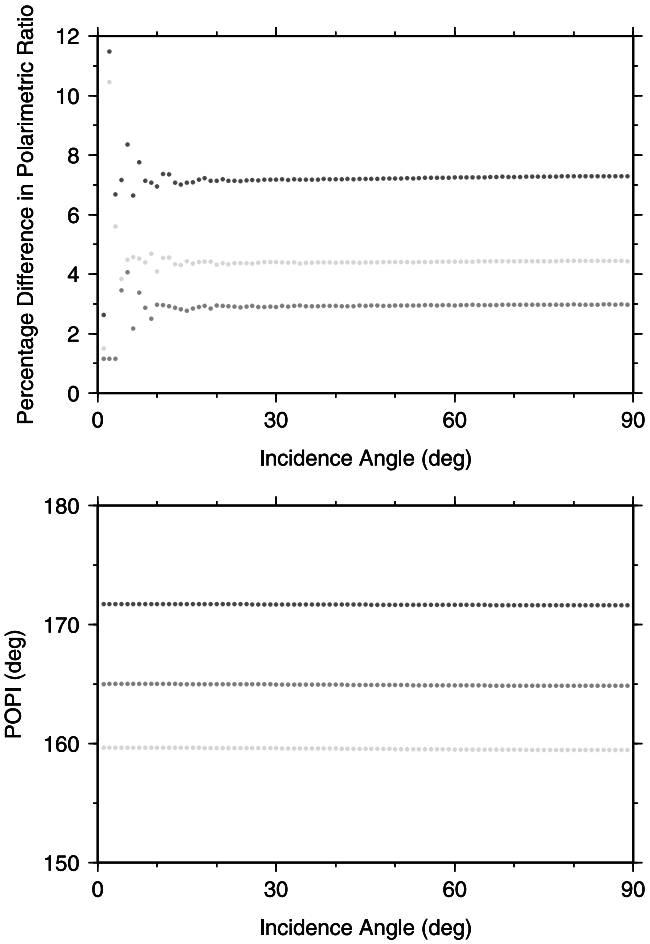

Figure 7. (top) The polarimetric ratio (PR), defined as the ratio between the copolar and the cross-polar Fresnel reflection coefficients, giving 100(sal1 − sal2)/sal1, for different salinity conditions at 15°C water temperature: dark grey, sal1 = 10 pps, sal2 = 40 pps; medium grey, sal1 = 10 pps, sal2 = 25 pps; light grey, sal1 = 25 pps, sal2 = 40 pps. (bottom) Polarimetric phase interferometry (POPI) values obtained from the Fresnel coefficients of water surface at 15°C and 10 pps (dark grey), 25 pss (medium gray), and 40 pss (light gray) salinity.

roughness. Therefore, the ratio of the two orthogonal polarizations excludes the roughness term and retains the dielectric effects [*Zavorotny and Voronovich*, 2000b; *Zavorotny et al.*, 2003]. The same references note that real data did not support this hypothesis. Some of the assumptions might be too crude, and better modeling is required.

[45] 3. The Object-identification (L.OI) approach was suggested by *Lie-Chung et al.* [2009] on the basis of a combination of computing the GNSS-R derived total reflectivity together with the carrier phase positioning of both up-looking and down-looking antennas.

3.4. Ice and Snow Applications

[46] For altimetric measurement over ice, see section 3.1. This section focuses on the techniques intended to characterize several other aspects of ice and snow, such as its permittivity (brine or temperature), texture, or substructure.

[47] Permittivity by peak-power (I.PP) obtains the effective dielectric constant empirically, as a function of the peak power [e.g., *Komjathy et al.*, 2000].

[48] For Vertical and the horizontal polarizations (I.VHP), *Zavorotny and Zuffada* [2002] suggested inferring the first-year thickness from the phase difference between the vertical and the horizontal polarized components.

[49] Similar to OP.PR, for Polarimetric Ratio (I.PR), the ratio between the amplitudes of both polarizations relates to variations in the permittivity of the sea ice (temperature and brine), especially at relatively low elevation angles of observation, around the Brewster angle. There is no algorithm in the literature, but Figure 8 shows the evolution of the polarimetric ratio captured over ~200 days, including the freezing and melting process of the sea ice in Disko Bay, Greenland.

[50] Permittivity POPI (I.POPI), as in OP.POPI, uses the phase difference between the copolar and cross-polar circular polarized components.

[51] For Sea ice roughness (I.R), *Belmonte* [2007] obtained the sea ice roughness by fitting the waveform shape.

[52] For Volumetric-scattering (S.V), *Wiehl et al.* [2003] suggested a volumetric scattering approach to model reflections produced in the subsurface firn layers of dry snow.

4. Models

[53] The set of models behind the GNSS-R data analysis are compiled in Table 5. Their application for this data set is detailed below.

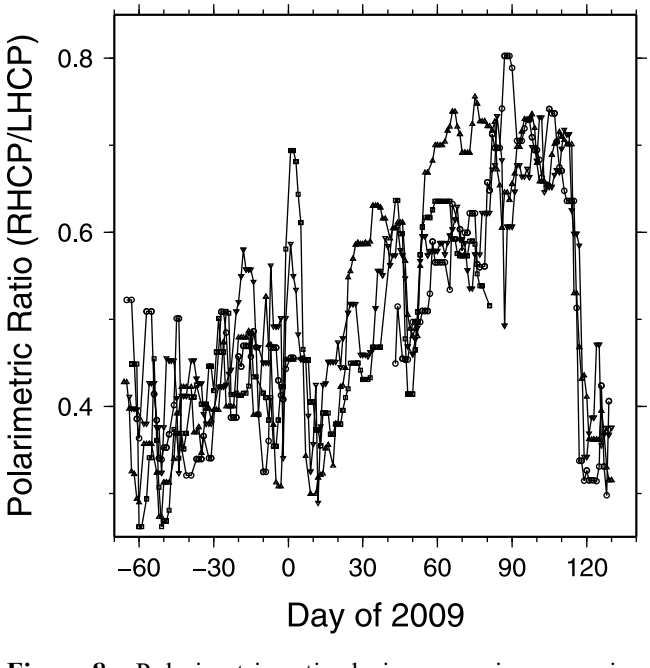

Figure 8. Polarimetric ratio during a sea ice campaign in Disko Bay, Greenland (GPS-SIDS-SI), as measured by different GPS satellites (PRN 2, 5, 17, and 20, shown by circles, squares, triangles, and inverted triangles, respectively) at ~13° elevation. The area had the presence of sea ice (more than 50% coverage) from mid-January 2009 to the beginning of May 2009. Short freezing events took place before ice was established.

Table 5. Examples of Waveform and Waveform Analysis Required Models[a]

Model	Notes
GNSS Bistatic Radar Equation	
General cross-polar DM, DDM	*Zavorotny and Voronovich* [2000a]
Convolution forms	*Garrison et al.* [2002], *Marchan-Hernandez et al.* [2008]
Linear in surface slopes PDF	*Cardellach and Rius* [2008]
EM Scattering Models	
KGO	*Zavorotny and Voronovich* [2000a]
KA	*Ulaby et al.* [1990]
SSA	*Voronovich* [1994]
SPM	*Rice* [1951]
Ice and Snow Scattering	
General	*Ulaby et al.* [1990]
Ice and snow	*Wiehl et al.* [2003]
Y1 sea ice	*Brown* [1982]
Dielectric Properties at L Band	
General	*Ulaby et al.* [1990]
Soil	*Vall-llossera et al.* [2005]
Sea ice	*Carsey* [1992], *Winebrenner et al.* [1989]
Sea Surface	
Wave spectrum	*Apel* [1994], *Elfouhaily et al.* [1997]
Slopes' distribution	Gaussian, binormal, Gram-Charlier; *Cox and Munk* [1954]
Range Corrections	
ρ_{geo}	$2H\sin(e)$; otherwise, see, e.g., *Wagner and Klokocnik* [2003] or ray tracers
ρ_{atm}	*Niell* [1996]
Multipath	*Townsend and Fenton* [1994], *Elosegui et al.* [1995], *Axelrad et al.* [1996]
Ray tracers	*Jones and Stephenson* [1975]
Clocks	not applicable for GOLD-RTR data
POPI Corrections	
Phase wind-up	*Wu et al.* [1993]

[a]There are problems for properly modeling the copolar component of the scattering. PDF, probability density function; KGO, Kirchhoff approximation at the geometric optics limit; KA, Kirchhoff approximation; SSA, small-slope approximation; SPM, small perturbation methods.

4.1. Altimetry and Ranges

[54] Section 3.1 presented different approaches to measure the altimetric range, i.e., the delay between the reflected and the direct radio links. In this section, range and delay will be both understood as in units of length (convert from time by the speed of light factor). The altimetric range is related to the vertical distance between the receiver and the reflecting surface, which in turn, and once the position of the receiver is precisely known, relates to the surface altitude with respect to an arbitrary reference (center of the Earth, a reference ellipsoid or geoid). In order to precisely know the receiver position, standard positioning techniques can be applied to the up-looking RHCP data. The data we provide already contain information about the up-looking antenna position. In some cases it is the postprocessing precise positioning whereas in some others is just the real-time solution given by GOLD-RTR's internal Novatel GPS receiver card (see Figure 2 for GOLD-RTR description). This can be checked in the global attributes of the data file.

[55] The general form of the altimetric equation is

$$r_{r-d} = \rho_{geo} + \rho_{atm} + \rho_{ins} + n \tag{1}$$

where r_{r-d} is the measured altimetric range (Table 2); n is the noise; ρ_{geo} is the geometric distance between the reflected and direct raypaths, if they both were collected at the well-positioned up-looking antenna. It depends on geometric parameters such as the altitude of the receiver above the reflecting surface H and incidence angle of observation; ρ_{atm} is the sum of the delays induced by the atmospheric conditions (troposphere, ionosphere); and ρ_{ins} includes instrumental biases, such as residual clock effects, cable lengths, and the antenna's offset vector (3-D vector between the up- and down-looking antennas). The antenna's offset vectors are provided in the data as global attributes and are given in the body frame reference system defined in Figure 9. In the integrated waveforms, the projection of these vectors into the direction of the observation (that is, the delay between the up and down antennas induced by the fact that their location are not coincident) is given in the variable EccentricityDelay, in meters (Table 4). Note that simultaneous observations from different satellites correspond to different values of this delay, because of their different azimuth and elevation angles of observation. Its convention sign is defined so that it must be subtracted to the measured altimetric range to obtain the total delay between the direct raypath and the reflected raypath that would have been received at the up-looking antenna position:

$$\rho_{ins} = \text{EccentricityDelay} \tag{2}$$

[56] The atmospheric corrections generally applied to GNSS navigation data are related to tropospheric and ionospheric effects. For GNSS-R at relatively low altitudes (such as the set of campaigns presented in this release), the ionospheric ones can be neglected, since both direct and reflected radio links are similarly affected. General models for the tropospheric delay induced in GNSS-like signals are given in the work by, e.g., *McCarthy and Petit* [2004] and *Spilker et al.* [1996], where the effect of the troposphere onto the GNSS delay is a function of several meteorological parameters. However, the delays induced by the tropospheric layer above the receiving platform cancel out, and only those due to the bottom layer, between the surface and the receiver, affect the altimetric range (this assumption fails for orbiting receivers). The variable AtmosphericDelay included in the provided integrated data (Table 4) is a simple model for ρ_{atm}, given in meters:

$$\rho_{atm} = \text{AtmosphericDelay} = \frac{4.6}{\sin(e)}\left(1 - e^{-\frac{H}{8621}}\right) \tag{3}$$

More complex models are given by *Niell* [1996], but they should be corrected to include solely twice the contribution below the receiver altitude ($\rho_{atm} = 2\rho_a^{bottom}$ in Figure 10).

[57] Multipath is a systematic effect altering the measured range. It consists in the interference of the radio link with

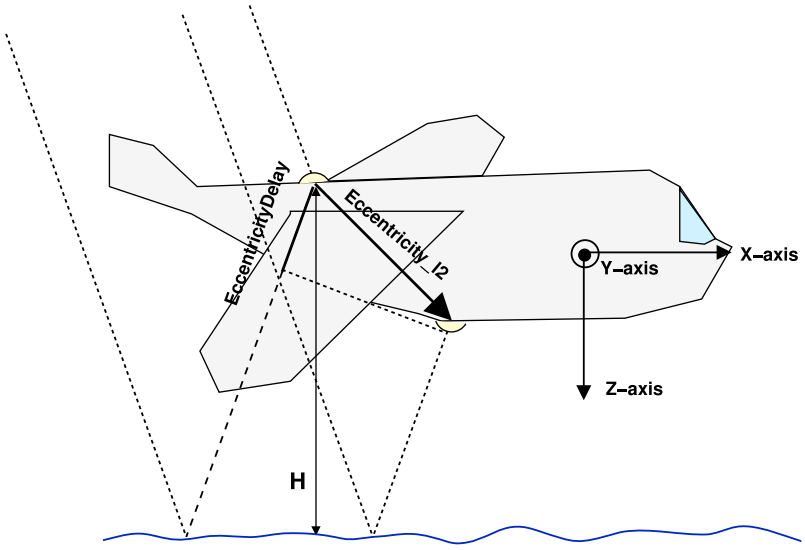

Figure 9. Sketch of the body frame coordinate system used to provide the offset vector between antennas (as global attributes). The fact that both up-looking and down-looking antennas are not located at the same point varies the delay, and this effect depends on the particular geometry of each observation.

its own reflections off surfaces near the receiver (such as aircraft wing and plates in airborne campaigns or tower pieces and other nearby equipment in ground-based experiments). Possible ways to detect, reduce, and correct it are given by, e.g., *Townsend and Fenton* [1994], *Elosegui et al.* [1995], and *Axelrad et al.* [1996]. Among the released data sets, Greenland observations are significantly affected by multipath.

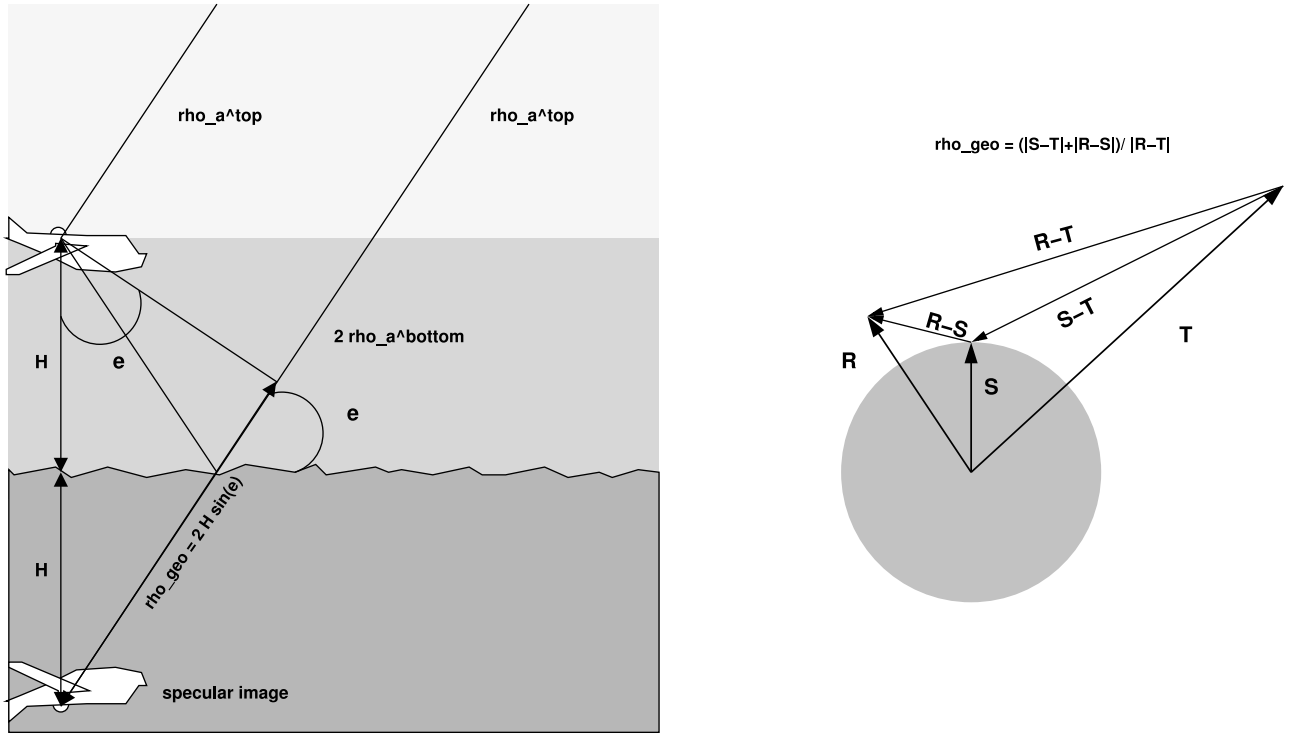

Figure 10. The altimetric range, the range difference between the direct and reflected raypaths, is a function of the altitude of the receiver above the surface H and the angle of observation e. It can be simply modeled assuming (left) parallel incidence and a flat surface or (right) a curved Earth, as provided in the GeometryDelay variable of the integrated data. At low receiving altitudes, the delays induced by the atmospheric layers above the receiver cancel out, whereas those induced by the bottom layer affect twice (shown in Figure 10, left). A simple correction for $\rho_{atm} = 2\rho_a^{bottom}$ is given in the data (equation (3)).

[58] The simplest form of ρ_{geo}, useful for relatively low receiver altitudes (such as most of these campaigns), assumes parallel incidence and flat surface (see Figure 10):

$$\rho_{geo} = 2H\sin(e) \tag{4}$$

where H is the altitude between the reflecting surface and the up-looking (well positioned) antenna, and e is the angle of elevation (complementary of the incidence angle). More accurate procedures take into account the curvature of the Earth, or even the actual shape of the geoid, on which the shortest reflected path and Snell reflection laws are applied to model the altimetric range [e.g., *Wagner and Klokocnik*, 2003]. The geometric model provided in our integrated data, under variable GeometryDelay (Table 4), is computed as

$$\rho_{geo} = \text{GeometryDelay} = \left(\left|\vec{R}-\vec{S}\right| + \left|\vec{S}-\vec{T}\right|\right) - \left|\vec{R}-\vec{T}\right| \tag{5}$$

with $\vec{R}$, $\vec{T}$, and $\vec{S}$ being the positions of the receiver, the transmitter, and the specular point on the curved Earth, respectively (Figure 10).

[59] As explained in section 3.1, the phase delay observations measure the variation in the altimetric range, $\Delta r_{r-d}(t)$. Hence, we can either obtain variations in the altitude with respect to the beginning of the continuous and connected carrier phases, ΔH (dynamic case), or the absolute value of H as $\Delta r_{r-d}(t)/2\Delta\sin(e)$.

[60] Finally, it is worth mentioning that for grazing angles of observation the signal crosses a long portion of the troposphere, whose gradients might bent the ray, changing both its altimetric delay and the atmospheric effects. Then, a better modeling involves ray tracers [e.g., *Jones and Stephenson*, 1975], systems that solve for the actual raypath as deduced from the Fermat's principle. The time taken by an electromagnetic wave to cross a media of refractive index n is

$$\tau = \int_S nds \tag{6}$$

where s is the path trough. Ray tracers find the path S such that minimizes the traveling time through a given atmospheric conditions n. For analysis of GNSS-R scenarios, the ray tracer must solve for both direct and reflected paths, differentiate them to get the modeled value of the altimetric range (with atmospheric effects included), compare with the measured range model, and iterate the procedure tuning the surface level, so that the measured altimetric ranges match the ray tracer modeled ones [*Cardellach et al.*, 2004].

4.2. Modeling the Waveform

[61] A general view of the theoretical basis of the GNSS-R is given by *Gleason et al.* [2009]. The waveform is usually modeled as done by *Zavorotny and Voronovich* [2000a], who provide the bistatic radar equation that includes the modulation of the signal by the PRN codes, as well as the Doppler filtering due to coherent integration. This model is based on the electromagnetic scattering in the Kirchhoff approximation at the geometric optics limit (KGO), valid for long surface correlation lengths and large vertical surface dispersion (relative to the wavelength). Extending the Zavorotny-Voronovich model to other electromagnetic scattering theories requires replacing the simple expression for the bistatic cross section in KGO by the more complex (numerically computed and tabulated) cross section corresponding to other models. Some of the alternative and more complete models suitable for L band scattering are (1) the full Kirchhoff approximation (KA) [e.g., *Ulaby et al.*, 1990], valid for small surface curvature (long surface correlation lengths compared to both wavelength and vertical dispersion), (2) the small-slope approximation (SSA) [e.g., *Voronovich*, 1994], applicable irrespective of roughness scales, as long as their slopes are small compared to the incident and scattering angles, and (3) two-scale models, in which a small-amplitude, high-frequency component is added and modeled by the small perturbation methods (SPM) [e.g., *Rice*, 1951] might be also used. As for deep snow or multilayer sea ice, the volumetric scattering has been modeled by *Wiehl et al.* [2003]. *Brown* [1982] developed a near-nadir scattering theory for first-year sea ice, which should be modified to accommodate the geometries (large incidence) of the released sea ice data sets. In order to speed up the computation of these models, the integral forms have been reformulated into more compact ways, such as convolution [*Garrison et al.*, 2002] and double convolution [*Marchan-Hernandez et al.*, 2008].

[62] *Ulaby et al.* [1990] give models for dielectric properties of several Earth surfaces (fresh and ocean waters, land, and different types of ice and snow). For L band specific permittivity values, *Blanch and Aguasca* [2004] and *Lang et al.* [2008] provide up-to-date measurements for seawater. For different soil types, recent L band measurements are given by *Vall-llossera et al.* [2005]. Microwave remote sensing of the sea ice is compiled by *Carsey* [1992]; dielectric and scattering-related properties are compiled by, e.g., *Winebrenner et al.* [1989].

[63] As for the modeling of the sea surface, the GNSS-R community usually takes the *Apel* [1994] or *Elfouhaily et al.* [1997] wave spectrum and Gaussian, binormal, or Gram-Charlier [*Cox and Munk*, 1954] distributions of the surface slopes.

5. Currently Available Data

[64] Figure 11 displays the geographic distribution of the released data, and their characteristics are summarized in Table 3. Each campaign permits different techniques among the ones listed in this paper. This information is also presented in Table 3, using the codes in Table 1. The server will be updated as new data sets are collected.

[65] The data provided in the server are in netCDF format (UNIDATA, http://www.unidata.ucar.edu/software/netcdf/index.html). Freely available libraries to deal with this format exist for several programming languages, such as C/C++ or f77/f90. GMT, IDL, or Matlab can also manipulate and display netCDF contents [e.g., *Wessel and Smith*, 1991].

[66] There are two types of files, containing integrated data (power waveforms) and raw data (complex waveforms). Raw data usage is detailed in the server documentation. For those users interested in how the receiver computes the raw waveforms, *Nogués-Correig et al.* [2007] give exhaustive details. The integrated data are the result of (1) a coherent sum of the raw complex waveforms, (2) the noncoherent sum

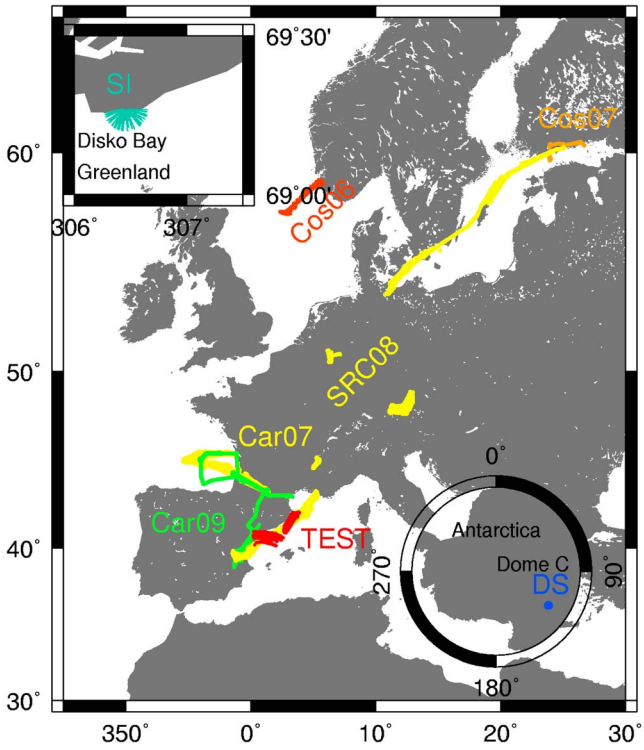

Figure 11. Map with the ground tracks of the released data. Different colors are used for different campaigns. Several flights and days of observations are available for each campaign.

of these waveforms (coherent and noncoherent integration length information self-contained in the data), (3) georeferencing the observations, and, finally, (4) computing some intermediate observables to facilitate the users' work (note that users can recompute those by themselves). Each georeferenced integrated-data file corresponds to either 1 flight, or 24 h observations in ground-based continuous monitoring campaigns. The variables contained in the georeferenced integrated data files are detailed in the Web server documentation. Here we compile some of them in Table 4, relevant for complementing and understanding some of the information provided in the article. They are flagged as level 1a or 1b to distinguish between values that cannot be reprocessed by the user (1a, given by the equipment or initial processing) and those that the user can recompute (1b). The combination of fields required to build different observables are explained in Table 2.

6. Summary and Conclusions

[67] The PARIS or GNSS-R techniques were suggested in early 90s, whereas most theoretical and experimental research about their potential applications emerged some years later. In this context, the Institut de Ciències de l'Espai designed and manufactured a dedicated GNSS-R hardware receiver, the GOLD-RTR, with which more than 40 airborne flights and 8 months ground-based campaigns were conducted over ocean, land, sea ice, and dry snow. Several aspects of the GNSS-R require further investigation, and new applications or approaches might be envisaged. For these reasons, the GNSS-R data collected since 2005 with the GOLD-RTR are made available to the research community. With the aim of encouraging new users and new research, the paper sought to review in an understandably manner the GNSS-R applications, techniques and algorithms that could be potentially applied to these data sets, together with the data structure, and the suitable models to deal with them.

[68] **Acknowledgments.** The campaigns and related studies have been supported by ESA/ESTEC (contracts 20069/06/NL/EL with CCN-1/CCN-2 and 21793/08/NL/ST), the CNES, and Spanish grant AYA2008-05906-C02-02/ESP. E.C. is under the Spanish Ramón y Cajal Program. Some precise trajectories have been produced at ICC, IdG, and GFZ.

References

Apel, J. (1994), An improved model of the ocean surface wave vector spectrum and its effects on radar backscatter, *J. Geophys. Res.*, *99*, 16,269–16,291.

Axelrad, P., C. Comp, and P. F. Macdoran (1996), SNR-based multipath error correction for GPS differential phase, *IEEE Trans. Aerospace Electron. Syst.*, *32*(2), 650–660.

Belmonte, M. (2007), Bistatic scattering of global positioning system signals from Arctic sea ice, Ph.D. thesis, Univ. of Colo. at Boulder, Boulder, Colo.

Blanch, S., and A. Aguasca (2004), Seawater dielectric permittivity model from measurements at L band, in *Proceedings of 2004 IEEE International Geoscience and Remote Sensing Symposium, IGARSS'04*, vol. 2, pp. 1362–1365, IEEE Press, Piscataway, N. J., doi:10.1109/IGARSS.2004.1368671.

Brown, G. S. (1982), A theory for near-normal incidence microwave scattering from first-year sea ice, *Radio Sci.*, *17*(1), 233–243, doi:10.1029/RS017i001p00233.

Cardellach, E., and A. Rius (2008), A new technique to sense non-Gaussian features of the sea surface from L-band bi-static GNSS reflections, *Remote Sens. Environ.*, *112*, 2927–2937, doi:10.1016/j.rse.2008.02.003.

Cardellach, E., G. Ruffini, D. Pino, A. Rius, A. Komjathy, and J. L. Garrison (2003), Mediterranean balloon experiment: Ocean wind speed sensing from the stratosphere using GPS reflections, *Remote Sens. Environ.*, *88*, 351–362.

Cardellach, E., C. Ao, M. de la Torre-Juárez, and G. Hajj (2004), Carrier phase delay altimetry with GPS-reflection/occultation interferometry from low Earth orbiters, *Geophys. Res. Lett.*, *31*, L10402, doi:10.1029/2004GL019775.

Cardellach, E., F. Fabra, O. Nogués-Correig, S. Oliveras, S. Ribó, and A. Rius (2009), From Greenland to Antarctica: CSIC/IEEC results on sea-ice, dry-snow, soil-moisture and ocean GNSS reflections, in *Proceedings of 2nd International Colloquium—Scientific and Fundamental Aspects of the Galileo Programme* [CD-ROM], edited by E. C. Bureau, Eur. Space Agency, Paris.

Carsey, F. (1992), *Microwave Remote Sensing of Sea Ice*, *Geophys. Monogr. Ser.*, vol. 68, 478 pp., AGU, Washington, D. C.

Cox, C., and W. Munk (1954), Measurement of roughness of the sea surface from photographs of the Sun's glitter, *J. Opt. Soc. Am.*, *44*, 838–850.

Delwart, S., C. Bouzinac, P. Wursteisen, M. Berger, M. Drinkwater, M. Martín-Neira, and Y. Kerr (2008), SMOS validation and the CoSMOS campaigns, *IEEE Trans. Geosci. Remote Sens.*, *46*, 695–704.

Elfouhaily, T., B. Chapron, K. Katsaros, and D. Vandemark (1997), A unified directional spectrum for long and short wind-driven waves, *J. Geophys. Res.*, *102*, 15,781–15,796.

Elfouhaily, T., D. R. Thompson, and L. Linstrom (2002), Delay-Doppler analysis of bistatically reflected signals from the ocean surface: Theory and application, *IEEE Trans. Geosci. Remote Sens.*, *40*, 560–573, doi:10.1109/TGRS.2002.1000316.

Elosegui, P., J. Davis, R. Jaldehag, J. Johansson, A. E. Niell, and I. Shapiro (1995), Geodesy using the Global Navigation System: The effects of signal scattering on estimates of site position, *J. Geophys. Res.*, *100*, 9921–9934, doi:10.1029/95JB00868.

Esterhuizen, S. (2010), GNSS receivers in space: From orbit determination to gravity field recovery (and a brief dabble in the affairs of SV49, GPS's black sheep), paper presented at Astrodynamics and Satellite Seminar,

Colo. Cent. for Astrodyn. Res., Univ. of Colo. at Boulder, Boulder, Colo., 20 Apr.
Garrison, J. L., A. Komjathy, V. U. Zavorotny, and S. J. Katzberg (2002), Wind speed measurement using forward scattered GPS signals, *IEEE Trans. Geosci. Remote Sens.*, *40*, 50–65.
Germain, O., G. Ruffini, F. Soulat, M. Caparrini, B. Chapron, and P. Silvestrin (2004), The eddy experiment: GNSS-R speculometry for directional sea-roughness retrieval from low-altitude aircraft, *Geophys. Res. Lett.*, *31*, L21307, doi:10.1029/2004GL020991.
Gleason, S. (2006), Remote sensing of ocean, ice and land surfaces using bistatically scattered GNSS signals from low Earth orbit, Ph.D. thesis, Univ. of Surrey, Surrey, U. K.
Gleason, S., S. Lowe, and V. Zavorotny (2009), *GNSS Applications and Methods*, chap. 16, pp. 399–436, Artech House, Boston, Mass.
Hajj, G., and C. Zuffada (2003), Theoretical description of a bistatic system for ocean altimetry using the GPS signal, *Radio Sci.*, *38*(5), 1089, doi:10.1029/2002RS002787.
Jones, R., and J. Stephenson (1975), A versatile three-dimensional ray tracing computer program for radio waves in the ionosphere, *OT Rep. 75-76*, Natl. Geophys. Data Cent., Boulder, Colo.
Katzberg, S., O. Torres, M. Grant, and D. Masters (2005), Utilizing calibrated GPS reflected signals to estimate soil reflectivity and dielectric constant: Results from SMEX02, *Remote Sens. Environ.*, *100*, 17–28, doi:10.1026/j.rse.2005.09.015.
Komjathy, A., J. Maslanik, V. U. Zavorotny, P. Axelrad, and S. J. Katzberg (2000), Sea ice remote sensing using surface reflected GPS signals, in *Proceedings of IEEE 2000 International Geoscience and Remote Sensing Symposium, IGARSS 2000*, pp. 2855–2857, IEEE Press, Piscataway, N. J.
Komjathy, A., M. Armatys, D. Masters, and P. Axelrad (2004), Retrieval of ocean surface wind speed and wind direction using reflected GPS signals, *J. Atmos. Oceanic Technol.*, *21*, 515–526.
Lagerloef, G., et al. (2008), The Aquarius/SAC-D mission: Designed to meet the salinity remote-sensing challenge, *Oceanography*, *21*, 68–81.
Lang, R., Y. Tarkocin, C. Utku, and D. L. Vine (2008), Accurate L-band dielectric constant measurements of seawater, in *Microwave Radiometry and Remote Sensing of the Environment, 2008. MICRORAD 2008*, pp. 1–4, IEEE Press, Piscataway, N. J., doi:10.1109/MICRAD.2008.4579507.
Lie-Chung, S., J. Jyh-Ching, T. Ching-Lang, C. Chia-Chyang, K. Ping-Ya, and T. Ching-Liang (2009), Stream soil moisture estimation by reflected GPS signals with ground truth measurements, *IEEE Trans. Instrum. Meas.*, *58*(3), 730–737, doi:10.1109/TIM.2008.2005821.
Lowe, S. T., C. Zuffada, Y. Chao, P. Kroger, L. E. Young, and J. L. LaBrecque (2002), 5-cm-precision aircraft ocean altimetry using GPS reflections, *Geophys. Res. Lett.*, *29*(10), 1375, doi:10.1029/2002GL014759.
Manandhar, D., R. Shibasaki, and H. Torimoto (2006), Prototype software-based receiver for remote sensing using reflected GPS signals, paper presented at 19th International Technical Meeting of the Satellite Division of the Institute of Navigation (ION GNSS 2006), Inst. of Navig., Fort Worth, Tex., 26–29 Sep.
Marchan-Hernandez, J., N. Rodriguez-Alvarez, A. Camps, X. Bosch-Lluis, I. Ramos-Perez, and E. Valencia (2008), Correction of the sea state impact in the L-band brightness temperature by means of delay-doppler maps of global navigation satellite signals reflected over the sea surface, *IEEE Trans. Geosci. Remote Sens.*, *46*, 2914–2923.
Martín-Neira, M. (1993), A Passive Reflectometry and Interferometry System (PARIS): Application to ocean altimetry, *ESA J.*, *17*, 331–355.
Martín-Neira, M., M. Caparrini, J. Font-Rosselló, S. Lannelongue, and C. S. Vallmitjana (2001), The PARIS concept: An experimental demonstration of sea surface altimetry using GPS reflected signals, *IEEE Trans. Geosci. Remote Sens.*, *39*, 142–149.
Masters, D., P. Axelrad, and S. Katzberg (2004), Initial results of land-reflected GPS bistatic radar measurements in SMEX02, *Remote Sens. Environ.*, *92*, 507–520, doi:10.1016/j.rse.2004.05.016.
McCarthy, D. D., and G. Petit (Eds.) (2004), IERS conventions (2003), *IERS Tech. Note 32*, 127 pp., Int. Earth Rotation and Ref. Syst. Serv., Frankfurt am Main, Germany.
McMullan, K., M. Brown, M. Martín-Neira, W. Rits, J. Marti, and J. Lemansczyk (2008), SMOS: The payload, *IEEE Trans. Geosci. Remote Sens.*, *46*, 594–605.
Miranda, J., M. Vall-llosera, A. Camps, N. Duffo, I. Corbella, and J. Etcheto (2003), Sea state effect on the sea surface emissivity at L-band, *IEEE Trans. Geosci. Remote Sens.*, *41*, 2307–2315.
Misra, P., and P. Enge (2006), *Global Positioning System: Signals, Measurements, and Performance*, Ganga-Jamuna, Lincoln, Mass.
Niell, A. (1996), Global mapping functions for the atmospheric delay at radio wavelengths, *J. Geophys. Res.*, *101*, 3227–3246, doi:10.1029/95JB03048.
Nogués-Correig, O., E. Cardellach Galí, J. Sanz Campderròs, and A. Rius (2007), A GPS-reflections receiver that computes Doppler/delay maps in real time, *IEEE Trans. Geosci. Remote Sens.*, *45*, 156–174.
Rice, S. (1951), Reflection of electromagnetic waves from slightly rough surfaces, *Commun. Pure Appl. Math.*, *4*(2–3), 351–378.
Rius, A., J. M. Aparicio, E. Cardellach, M. Martín-Neira, and B. Chapron (2002), Sea surface state measured using GPS reflected signals, *Geophys. Res. Lett.*, *29*(23), 2122, doi:10.1029/2002GL015524.
Rius, A., E. Cardellach, and M. Martín-Neira (2010), Altimetric analysis of the sea surface GPS reflected signals, *IEEE Trans. Geosci. Remote Sens.*, *48*(4), 2119–2127, doi:10.1109/TGRS.2009.2036721.
Rodriguez-Alvarez, N., et al. (2011), Land geophysical parameters retrieval using the interference pattern GNSS-R technique, *IEEE Trans. Geosci. Remote Sens.*, *49*, 71–84, doi:10.1109/TGRS.2010.2049023.
Ruffini, G., F. Soulat, M. Caparrini, O. Germain, and M. Martín-Neira (2004), The eddy experiment: Accurate GNSS-R ocean altimetry from low altitude aircraft, *Geophys. Res. Lett.*, *31*, L12306, doi:10.1029/2004GL019994.
Semmling, A. M., et al. (2011), Detection of Arctic Ocean tides using interferometric GNSS-R signals, *Geophys. Res. Lett.*, *38*, L04103, doi:10.1029/2010GL046005.
Soulat, F., M. Caparrini, O. Germain, P. Lopez-Dekker, M. Taani, and G. Ruffini (2004), Sea state monitoring using coastal GNSS-R, *Geophys. Res. Lett.*, *31*, L21303, doi:10.1029/2004GL020680.
Spilker, J. J., B. W. Parkinson, P. Axelrad, and P. Enge (Eds.) (1996), *Global Positioning System: Theory and Applications*, Am. Inst. of Aeronaut. and Astronaut., Washington, D. C.
Townsend, B., and R. Fenton (1994), A practical approach to the reduction of pseudo-range multipath errors in an L1 GPS receiver, paper presented at 7th International Technical Meeting of the Satellite Division of the U.S. Institute of Navigation (ION GPS 1994), Inst. of Navig., Salt Lake City, Utah, 20–23 Sep.
Treuhaft, R. N., S. T. Lowe, C. Zuffada, and Y. Chao (2001), Two-cm GPS altimetry over Crater Lake, *Geophys. Res. Lett.*, *28*(23), 4343–4346.
Ulaby, F., R. Moore, and A. Fung (1990), *Microwave Remote Sensing: Active and Passive*, vol. 3, Artech House, Boston, Mass.
Valencia, E., J. F. Marchan-Hernandez, A. Camps, N. Rodriguez-Alvarez, J. M. Tarongi, M. Piles, I. Ramos-Perez, X. Bosch-Lluis, M. Vall-llossera, and P. Ferre (2009), Experimental relationship between the sea brightness temperature changes and the GNSS-R delay-Doppler maps: Preliminary results of the albatross field experiments, in *Proceedings of Geoscience and Remote Sensing Symposium 2009, IGARSS 2009*, vol. 3, pp. III-741–III-744, IEEE Press, Piscataway, N. J., doi:10.1109/IGARSS.2009.5417871.
Valencia, E., A. Camps, J. F. Marchan-Hernandez, N. Rodriguez-Alvarez, I. Ramos-Perez, and X. Bosch-Lluis (2010), Experimental determination of the sea correlation time using GNSS-R coherent data, *IEEE Geosci. Remote Sens. Lett.*, *7*(4), 675–679, doi:10.1109/LGRS.2010.2046135.
Vall-llossera, M., M. Cardona, S. Blanch, A. Camps, A. Monerris, and I. Corbella (2005), L-band dielectric properties of different soil types collected during the MOUSE 2004 field experiment, in *Proceedings of 2005 IEEE International Geoscience and Remote Sensing Symposium, IGARSS'05*, vol. 2, pp. 1109–1112, IEEE Press, Piscataway, N. J., doi:10.1109/IGARSS.2005.1525309.
Voronovich, A. G. (1994), Small-slope approximation for electromagnetic wave scattering at a rough interface of two dielectric half-spaces, *Waves Random Media*, *4*, 337–367.
Wagner, C., and J. Klokocnik (2003), The value of ocean reflections of GPS signals to enhance satellite altimetry: Data distribution and error analysis, *J. Geod.*, *77*, 128–138.
Wessel, P., and W. H. F. Smith (1991), Free software helps map and display data, *Eos Trans. AGU*, *72*(41), 441.
Wiehl, M., R. Légrésy, and R. Dietrich (2003), Potential of reflected GNSS signals for ice sheet remote sensing, *Prog. Electromagn. Res.*, *40*, 177–205.
Winebrenner, D., L. Tsang, B. Wen, and R. West (1989), Sea-ice characterization measurements needed for testing of microwave remote sensing models, *IEEE J. Oceanic Eng.*, *14*(2), 149–158, doi:10.1109/48.16828.
Wu, J., S. Wu, G. Hajj, W. Bertiger, and S. Lichten (1993), Effects of antenna orientation on GPS carrier phase, *Manuscripta Geod.*, *18*(2), 91–98.
Zavorotny, V. U., and A. G. Voronovich (2000a), Scattering of GPS signals from the ocean with wind remote sensing application, *IEEE Trans. Geosci. Remote Sens.*, *38*, 951–964.
Zavorotny, V. U., and A. G. Voronovich (2000b), Bistatic GPS signal reflections at various polarizations from rough land surface with moisture content, in *Proceedings of IEEE 2000 International Geoscience and Remote Sensing Symposium, IGARSS 2000*, vol. 7, pp. 2852–2854, IEEE Press, Piscataway, N. J., doi:10.1109/IGARSS.2000.860269.

Zavorotny, V., and C. Zuffada (2002), A novel technique for characterizing the thickness of first-year sea-ice with the GPS reflected signal, *Eos Trans. AGU*, *83*(47), Fall Meet. Suppl., Abstract C11A-0980.

Zavorotny, V. U., D. Masters, A. Gasiewski, B. Bartram, S. Katzberg, P. Axelrad, and R. Zamora (2003), Seasonal polarimetric measurements of soil moisture using tower-based GPS bistatic radar, in *Proceedings of IEEE 2003 International Geoscience and Remote Sensing Symposium, IGARSS 2003*, vol. 2, pp. 781–783, IEEE Press, Piscataway, N. J., doi:10.1109/IGARSS.2003.1293916.

E. Cardellach, F. Fabra, O. Nogués-Correig, S. Oliveras, S. Ribó, and A. Rius, Institut de Ciències de l'Espai, CSIC/IEEC, Campus UAB, Torre C5-par, 2on pis, Bellaterra, E-08193 Barcelona, Spain. (estel@ieec.uab.es)